EXPERIMENTAL INVESTIGATIONS OF THE AERODYNAMIC CHARACTERISTICS OF MOVING MIRCO AIR VEHICLE WINGS

T.J. Möller, R. Wokoeck, M. Emge, J. Schüssler, R. Radespiel
Institut für Strömungsmechanik, Technische Universität Braunschweig
Bienroder Weg 3, 38106 Braunschweig, Deutschland

Abstract

A new experimental test environment to investigate the unsteady aerodynamic properties of micro air vehicles (MAV) (i.e. forces, moments and flow field) is introduced. This test rig is designed for wind tunnel testing of 1:1 scale MAVs. The development of such small vehicles needs investigations of their behaviour under realistic but also clearly defined, repeatable flow conditions simulating dynamic flight. The new setup is capable to measure the unsteady aerodynamic forces whilst performing an arbitrary controlled motion with 3 degrees of freedom in the upright Y=0 plane. These include typical flapping wing motions like plunging, pitching and their combinations as well as transients to simulate sudden gusts. Dynamic measurements for plunge and pitch motion were performed to determine the dynamic derivatives of a moving MAV wing model.

1. Nomenclature

AR	aspect ratio=s^2/A
A	wing area
$c_{Mq} + c_{M\dot{\alpha}}$	pitch damping coefficient
c_D	drag coefficient
c_L	lift coefficient
c_M	pitch coefficient
f	frequency
h	plunge amplitude
k	reduced frequency = $\frac{\pi f c}{U_\infty}$
l_μ	reference length
M_y	pitch moment
$M(t)$	balance signal
q_∞	stagnation pressure
U_∞	free stream velocity
s	wing span
z_1	amplitude of plunge motion
α	angle of attack
α_0	mean angle of attack
α_1	pitch amplitude
α_{eff}	Amplitude effective angle of attack = $2k\frac{z_1}{l_\mu}$
β	angle of yaw
κ, λ, μ	coefficients from Fourier series
ρ	density
$\Theta(t)$	position signal

2. INTRODUCTION

The aerodynamics of micro air vehicles (MAVs) in the low speed regime differs considerable from the aerodynamics of larger vehicles, e.g. Unmanned Air Vehicle (UAV). To improve the understanding of the flow phenomena occurring in the low Reynolds number regime, it is useful to conduct experiments under realistic flight conditions and to provide experimental data for comparisons with CFD results. For recently developed MAVs, Reynolds numbers about Re= 5 x 10^4 – 2 x 10^5 characterise the typical regime [1].

Typical MAV geometries are presented by Lian et al. [2]. They use a flexible wing and present a numerical method to optimize the performance of the wing. They choose the optimum from mean aerodynamic coefficients. Grasmeyer et al. [3] present a MAV with rigid wing. Flows in low Reynolds number regime are analysed applying numerical methods by Ekaterinaris et al. [4]. Their focus is on the simulation of the transitional flow features of the flow over a NACA 0012 airfoil. Ramamurti et al. [5] present a simulation of several realised MAV configurations. They report on the effect of geometry and angle of attack on the steady aerodynamic coefficients. Swanson and Issac [6] present numerical results on the aerodynamics of wings for MAVs for high angles of attack. Sunda and Sakaguchi [7] report on the unsteady forces on a 2d wing in pitch and plunge motion but give no unsteady aerodynamics coefficients for the investigated configuration. Only little is published for unsteady aerodynamics of MAV wings and the relevant flow regimes.

The validation of numerical results at such low Reynolds numbers and especially for the unsteady aerodynamics is very difficult due to the low resulting forces. Therefore a specially built test facility for this flow regime is introduced

in the present work. The experimental environment is capable of simulating the unsteady aerodynamics of MAVs. A way to determine dynamic stability parameters is presented by Hübner [8] and applied to wings large aspect ratio wings. This approach is used in the same way for MAV wings with small aspect ratio in the present paper.

3. EXPERIMENTAL SET UP

A new test section of the LNB is designed and built for wind tunnel testing of 1:1 scale MAV. The development of such small vehicles needs investigations of their behaviour under realistic but also clearly defined, repeatable situations that may encounter the vehicle during flight. The test rig is capable of measuring the aerodynamic forces and moments whilst performing a controlled motion with 3 degrees of freedom in the upright Y=0 plane including flapping wing motions like plunging, pitching and their combinations and transients simulating sudden gusts or crosswinds.

3.1. Wind tunnel

The LNB is a continuous atmospheric Eiffel-type wind tunnel with a closed test section. The settling camber with nozzle, the diffuser and the motor mounting are made from glass fibre reinforced epoxy and the test section is transparent for using optical measurement techniques. A 3 kW motor drives the tunnel in suction mode, which gives a maximum flow velocity of 19 m/s and a turbulence level Tu <0.% at 10 m/s. The velocity varies less than 1% over the cross section. The wind tunnel is installed in a 8.2 m long room, which allows circulation of the flow. The ceiling of the room is covered with open-cell acoustic foam to damp noise. To minimize vibrations, the wind tunnel is mounted on rubber absorbers that are fastened on a steel construction. Motor and fan are decoupled from the rest of the tunnel.

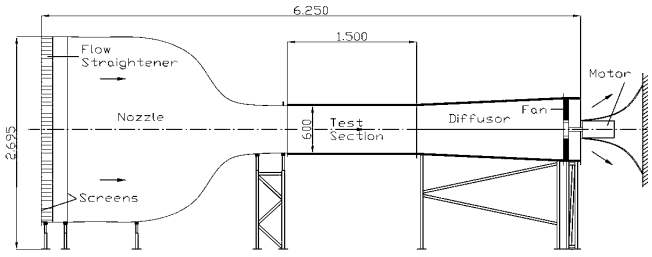

Fig. 1. Sketch of wind tunnel LNB

3.2. Model support

The model support is designed for the measurement of 3D aerodynamic models during high dynamic and high precision movements with 3 degrees of freedom in the upright plane.

The model support is driven by linear synchronous direct drives with moving coil, each consuming a maximum of 1950 W transferred into a maximum of 700 N or a speed of 5.3 m/s, during high dynamic and high precision movements. The standard movements are a plunging motion up to ±150 mm @ 3 Hz and a pitching motion with max. ±20° @ 3 Hz. The position accuracy is ±0.1mm or ±0.1°: The repetitive accuracy of both types of motion is ±0.05mm or ±0.1°.

A sketch of the actuation principle is shown in fig. 2. The two actuators named *a* are used to create pitch and plunge motion of the model. The established set up generally causes a small longitudinal motion in *x*-direction. To remove this problem additional actuators named *b* will be added in a next step to optimise the test rig. Fig. 3 shows the assembled actuator setup in the wind tunnel downstream of the test section.

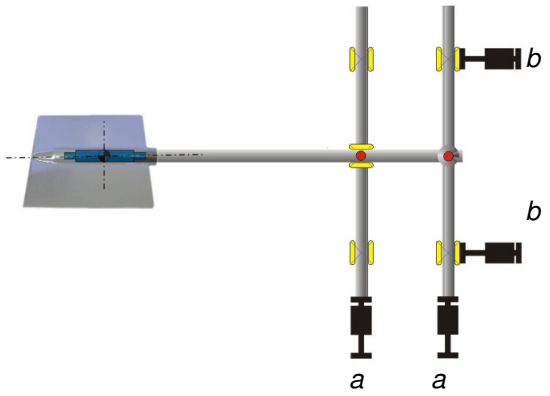

Fig. 2. Sketch of actuation principle of model support

Fig. 3. Picture of model support applied in wind tunnel

To prescribe the movement of the two linear drives the planned model motion is created by using a CAD tool. With this tool the motion of the model is simulated and the coordinates of the resulting movement of the two motors are exported as an ASCII file. This file is converted by a specially designed program to the format of the programmable logic controller (PLC) of the linear motors. This method allows a precise and flexible setting of the model motion.

While moving the sting has a natural bending mode of a typical frequency of around 37 Hertz. This frequency is

found in the balance signal. Therefore this component of the balance signal has to be removed by data processing during the data evaluation.

To assure the wind tunnel model and hence the wind tunnel balance will not contact the walls of the test section different actions are implemented to prevent this kind of accident. Light barriers are installed to stop immediately the motion of the motors if the model moves below a certain defined distance to the wall. A second measure is a fine wire which is destroyed if the angle of attack of the model is bigger than a defined value. This will also stop the motion of the motors promptly.

3.3. Wind tunnel balance and measurement system

A very small, specially designed six component internal strain gauge balance is used to determine the aerodynamic forces. The dimensions of the balance are 107 mm in length and 11.2 mm in diameter with a weight of 35g. The specifications are given in tab 1. Fig. 4 shows a picture of the balance.

F_x : ± 7 N	M_x : ± 0.75 Nm
F_y : ± 20 N	M_y : ± 0.75 Nm
F_z : ± 20 N	M_z : ± 0.374 Nm

Tab 1. wind tunnel balance measurement range

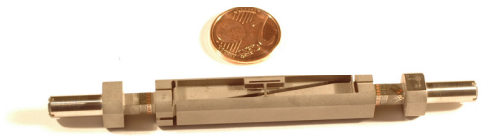

Fig. 4. Wind tunnel balance

The balance and a Hottinger Baldwin Messtechnik MGCplus strain amplifier were used to measure the dynamic forces and moments on the MAV wings. The overall accuracy of the balance is better than 0.025% FS.

3.3.1. Wind tunnel model

For the first measurements two types of MAV models have been built. The first are rigid and flexible platforms using a 7.42% cambered profile to study the interaction between aerodynamics and wing deformation (s. fig.5 and 6). A similar profile is used in [1].

The second type is a set of two flat plate wings varying in aspect ratio (s. fig.7) to investigate the influence of Reynolds number and aspect ratio. They have a chord length c=117 mm, spans s=117mm and 234mm, and their thickness is 2.7 mm while all edges are rounded with r=1.35mm

Both types of MAV wings are designed to be equipped with the internal balance described above.

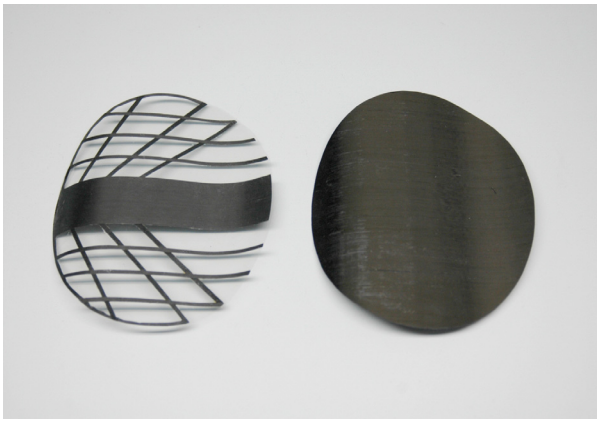

Fig. 5. MAV wing platforms: flexible (left) and rigid (right).

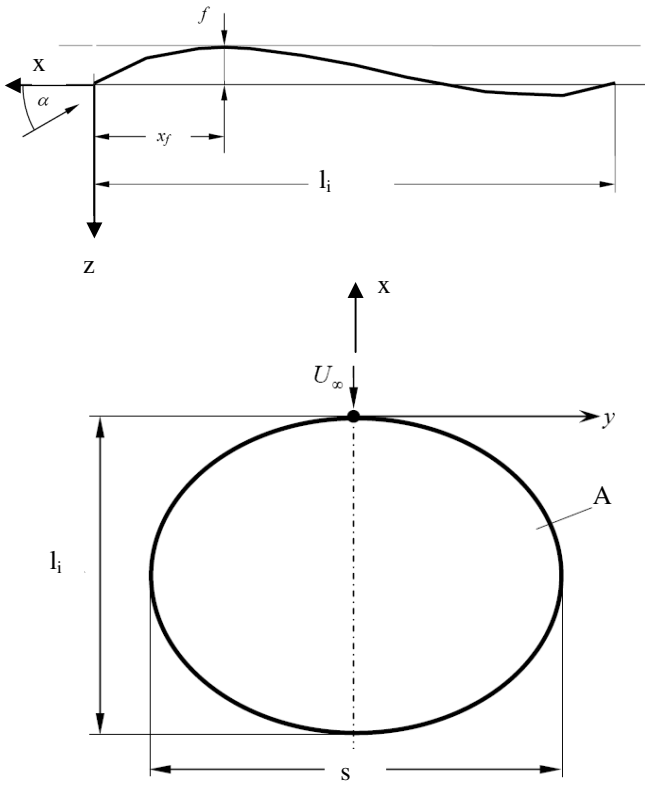

Fig. 6. Geometry of cambered wing
s=150mm l_i=l_μ=120mm f= 8.9mm x_f=30mm

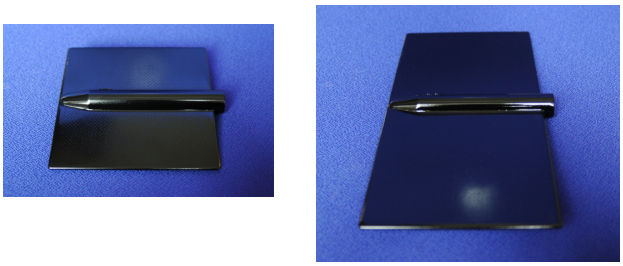

Fig. 7. Flat plate MAV wing with aspect ratio AR = 1 (left) and AR =2 (right).

4. DATA EVALUATION

The derivatives were calculated using the assumption the aerodynamic forces and moments are linear functions of model position and angular speed. This assumption is valid for attached flows and for low angles of attack. If this is not the case more sophisticated models [9] have to be established.

Furthermore the MAV wings are assumed to be ideally stiff, hence no elasticity effects are considered under this assumption. Moreover the tests presented here have been conducted for β=0**.**

To eliminate added mass and inertial forces measurements with wind-on conditions are performed with exactly the same conditions in wind-off conditions. The wind-on and wind-off balance data are then subtracted, after averaging the raw data (s. fig 8) over 80 periods (s. fig. 9). After the averaging over 80 cycles still high frequency perturbations caused by the harmonics of the natural vibration of the actuator mechanism can be seen on the signal. To remove this perturbation from the signal a low pass Bessel filter is applied (s. fig. 10).

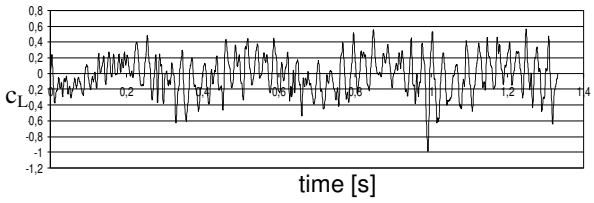

Fig. 8. Example c_L as a function of time (raw data)

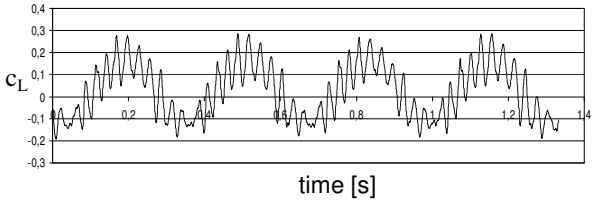

Fig. 9. Example c_L as a function of time (averaged data)

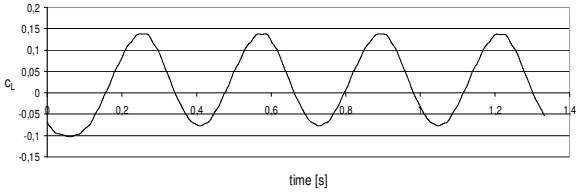

Fig. 10. Example c_L as a function of time (low pass Bessel filter)

The position data is processed in the same way.

The determination of dynamic derivatives from the data of unsteady pitching motion is given as an example here:

$$c_{Mq} + c_{M\dot{\alpha}}$$

Here c_{Mq} is the quasi-steady term and represents the pitch moment c_M due to constant pitching rates. $c_{M\dot{\alpha}}$ is an unsteady term, representing the influence of wake of the MAV wing.

The derivatives are calculated from balance and position signals which both are recorded by the MGCplus amplifier. The position signal $\Theta(t)$ and the balance signal Z(t) can be expressed as a Fourier series. The balance signal can be written as

$$Z(t) = Z_0 + \sum_{n=1}^{\infty}\left(Z_{C,n} \cdot \cos(n\omega t) + Z_{S,n} \cdot \sin(n\omega t)\right)$$

Regarding only the fundamental frequency ϖ reduces the above equation to

$$Z(t) = Z_0 + Z_{\cos} \cdot \cos(\omega t) + Z_{\sin} \cdot \sin(\omega t)$$

In fig. 11 the filtered signal of c_M over time is shown. The reconstructed lapse of c_M is presented in fig. 12. It can be seen the reconstructed signal correlates well the filtered one.

The pitching moment is composed of a constant part, a part which is proportional to the position signal $\Theta(t)$ and a part which is proportional to the rotational speed $\dot{\Theta}(t)$. The pitching moment may be expressed as:

$$M(t) = \kappa + \lambda \cdot \Theta(t) + \mu \cdot \dot{\Theta}(t)$$

The coefficients κ, λ and μ are obtained from the Fourier series $\Theta(t)$ and M(t). With these coefficients the pitch damping can be determined:

$$c_{Mq} + c_{M\dot{\alpha}} = \frac{\mu}{\frac{l_\mu}{U_\infty} q_\infty \cdot A \cdot l_\mu} - \frac{\frac{d_l}{l_\mu}\lambda}{q_\infty \cdot A \cdot l_\mu}$$

Here d_l is the distance between the motion centre and the moment reference point. The detailed derivation of the coefficients κ, λ and μ are presented in [10] and reported in full detail in [11] .

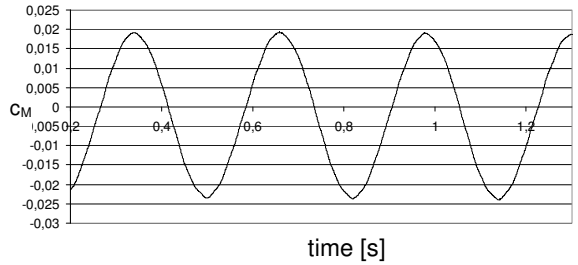

Fig. 11. Filtered lapse of c_M as a function of time

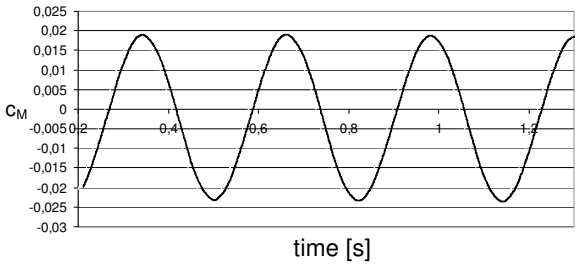

Fig. 12. Reconstructed lapse of c_M as a function of time

5. EXPERIMENTAL RESULTS

Static measurements were conducted to investigate the influence of the Reynolds number, the angle of attack and the stiffness of the structure for flow over the cambered wings. Dynamic measurements for plunge and pitch motion were performed to determine the dynamic derivatives of the MAV models. In this paper results for the flow with Re_c=36000 and Re_c=72000 are presented.

5.1. Static measurements

In a first step the two cambered MAV wings were investigated to demonstrate the reliability of the new simulation facility and display the influence of the stiffness of the structure on the coefficients and the drag polar.

The distribution of drag and lift coefficients are shown in fig. 13. It can be seen similar results are found in the actual measurements compared to those presented in [1].

Lift and drag coefficients for the different Reynolds numbers are presented in fig 14. It is seen that the higher Reynolds number yields larger maximum lift coefficients. Note the balance is surprisingly sensitive for drag measurements as zero lift drag for Re=36000 was only 0.021N. Moment coefficients for different Reynolds numbers are shown in fig. 15. It can be noticed mainly the pitching moment c_M is influenced noticeable by increasing the Reynolds number. The other moment like yawing c_N and roll moment c_L are only little influenced by the increasing Reynolds number.

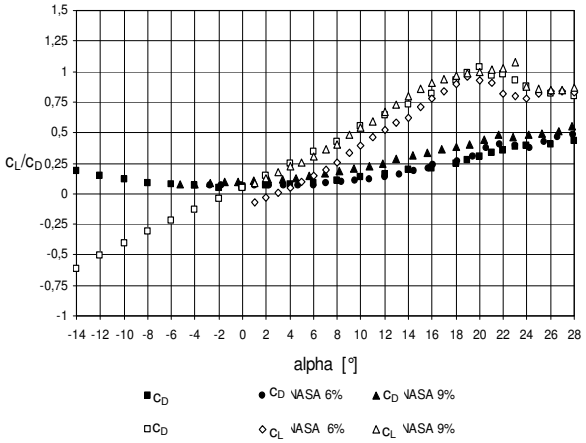

Fig. 13. Force coefficients versus α for stiff wing in comparison with measurements [1], Re=72000

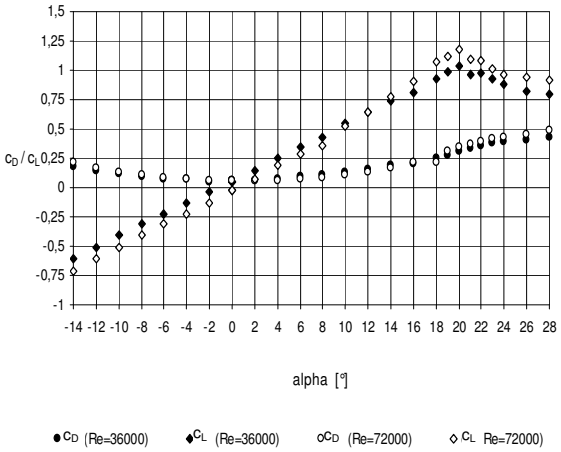

Fig. 14. Drag and lift coefficients for stiff cambered wing Re=36000 and Re=72000

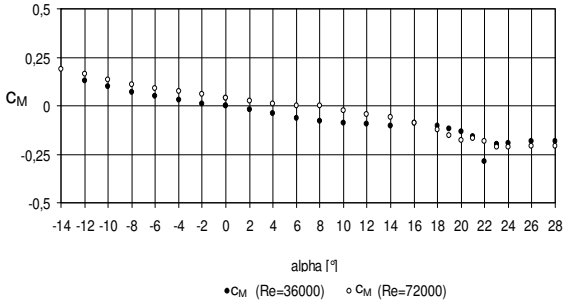

Fig. 15. Moment coefficients with respect to the quarter cord line for stiff cambered wing Re=36000 and Re=72000

The influence of the deformable structure of the wing is shown in fig. 16 and 17 for two Reynolds numbers. Note the dynamic pressure was four times larger at the larger Reynolds number.

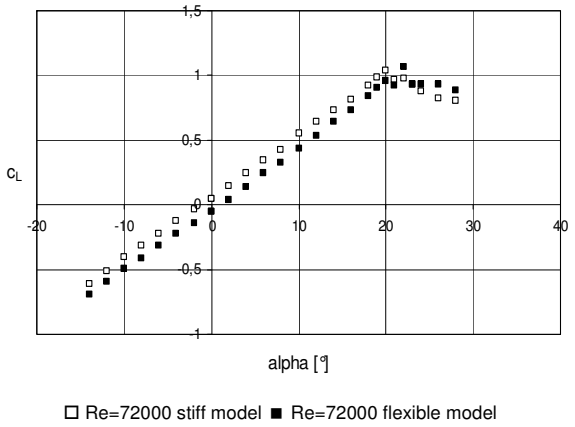

Fig. 16. Lift coefficients for stiff and flexible cambered wing Re=36000

Due to the deformation of the flexible wing the stall is delayed and also the slope of $\frac{dc_L}{d\alpha}$ is decreasing with increasing flexibility of the wing.

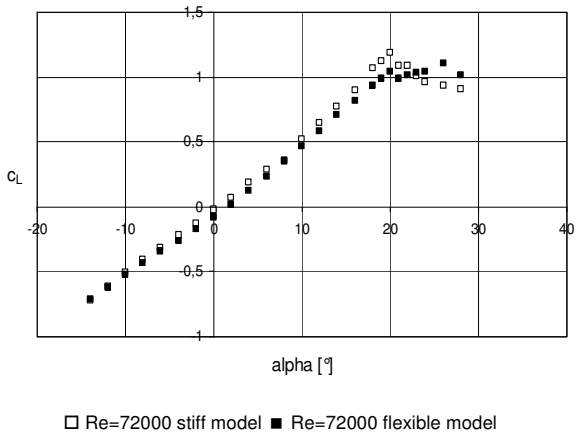

Fig. 17. Lift coefficients for stiff and flexible cambered wing Re=72000

5.2. Results of dynamic measurements

From the range of dynamic measurements performed so far the results of two specific motions are investigated. The first motion is a harmonic pitch motion with α_1 = 5.8877° abd with α_0 = 0 and α_0 = 8°, respectively. The second motion is a harmonic plunging motion with an amplitude h=24mm and 48mm and with α_0=0 and α_0=8°, respectively. The dynamic measurements are performed with the flat-plate models.

The pitching motion about the mean value α_0 with amplitude of α_1 generates a hysteresis loop in the aerodynamic response. This is shown in fig. 18 and 19 for aspect ratio 1:1 and 1:2 respectively. The static slope for the increase of lift based on the theory of Truckenbrodt [12] is also shown in fig. 18 and 19.

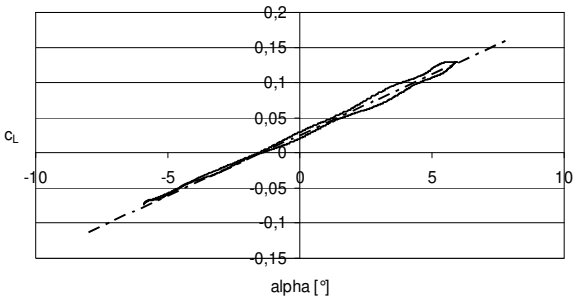

Fig. 18. c_L versus α (5 Hz low pass filter) f=3.13 Hz, U_∞=4.62m/s, α_0=0°, AR=1:1, Re=36000, k=0.25

——— measurements
- · - · - theory Truckenbrodt [12]

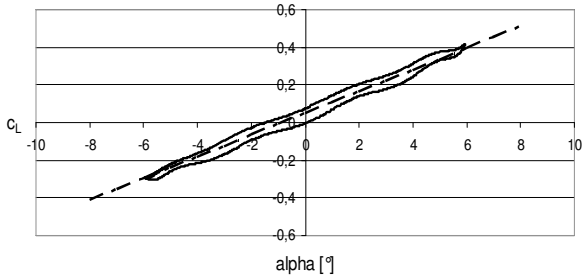

Fig. 19. c_L versus α (5 Hz low pass filter), f=3.13Hz, U_∞=4.62m/s, ,α_0=0, AR=2:1 Re=36000, k=0.25

——— measurements
– – – theory Truckenbrodt [12]

The non zero lift for α=0 indicates the model was not oscillating symmetrically around zero angle of attack during pitching motions. This problem was traced back to a misalignment of the two linear drives during the dynamic test. The misalignment can be removed in future applications of the model support.

The effect of the aspect ratio on the dynamic coefficients can be seen in the width of the hysteresis loop presented in fig. 20 and 21, respectively.

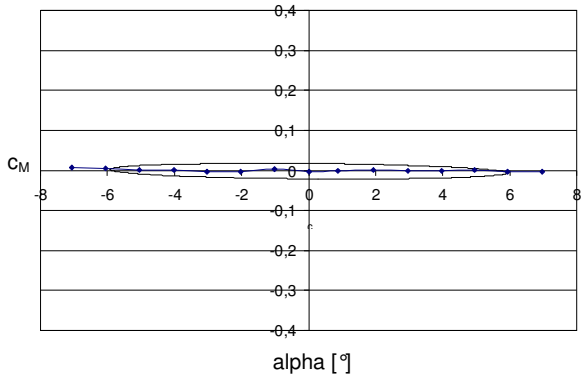

Fig. 20. Pitch moment versus α (5 Hz low pass filter), f=3.13Hz, U_∞=4.62m/s, ,α_0=0, AR=1:1 Re=36000, k=0.25

——— Dynamic measurements
— · · · static measurements

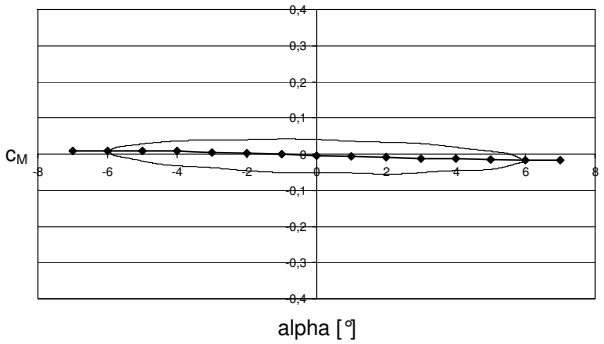

Fig. 21. Pitch moment versus α (5 Hz low pass filter), f=3.13Hz, U_∞=4,62m/s, α_0=0, AR=2:1 Re=36000, k=0.25

——— Dynamic measurements
– · – – · static measurements

With this data the unsteady aerodynamic derivatives were calculated following the method presented above. The results are shown in tab. 2. The experimental data has also been evaluated by the method discussed in [8]. This method leads to the same numerical result. For pitching motion with α_0=0 and 8° the pitch damping increases with the wing aspect ratio.

AR \ α_0	0°	8°
1:1	-0.3618	-0.3964
2:1	-1.2601	-1.2012

Tab 2. Pitch damping coefficients for pitching motion Re=36000, k=0.25

The values of the static measurements with corrected angle of attack are also given in fig. 20 and 21. These values show a good alignment with the dynamic measurements.
Furthermore additional tests have been performed with decreasing *k* to test if the dynamic data converge towards the static results for decreasing motion frequency. It is found that the dynamic results come up to the static results.

The value of $c_{M\dot{\alpha}}$ is shown in tab. 3 for α_0=8° and for an aspect ratio of 1 and 2:

AR \ α_0	8°
1:1	-0.2490
2:1	-0.5834

Tab 3. $c_{M\dot{\alpha}}$ for plunging motion Re=36000,k=0.25

Fig 22 shows the effective angle of attack α_{eff} and the pitch moment coefficient c_M for AR=1 and 2 as a function of time for plunging motion. It can be seen the phase shift for the two different aspect ratios with respect to α_{eff} are different. The phase shift is decreasing with decreasing aspect ratio. This indicates an also decreasing pitch damping which is found in the data shown in tab. 3.

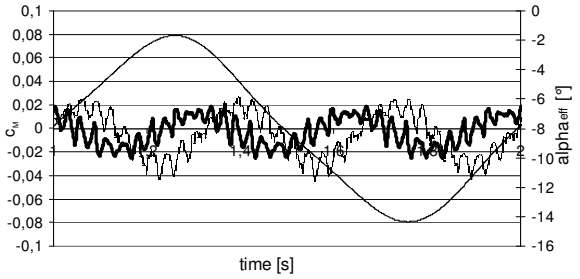

Fig. 22. α_{eff} and c_M versus time (average), U_∞=4,62m/s, α_0=8°, Re=36000, k=0.25

——— α_{eff}
····· c_M AR=1
——— c_M AR=2

Finally using the potential flow method presented by Laschka [13] we obtain theoretical values for the amplitude of the unsteady lift and pitch moment coefficient and the corresponding phase shift for AR=2. This data is used together with the harmonic position signal to determine the pitch damping $c_{Mq} + c_{M\dot{\alpha}}$, thereby applying the actual presented data evaluation method. Fig. 23 shows the comparison of the present measurement for aspect ratios 1 and 2 ad Reynolds numbers 36000 and 72000 to the potential flow data. While the measurements and the potential flow model are in good agreement for an aspect ratio of 2 there is a rapid decrease of measured pitch damping coefficient for small AR. Note is was not easily possible to extract theoretical results for AR=1 from [13]. It is found the influence of the Reynolds number on the pitch damping is smaller than the effect of the aspect

ration.

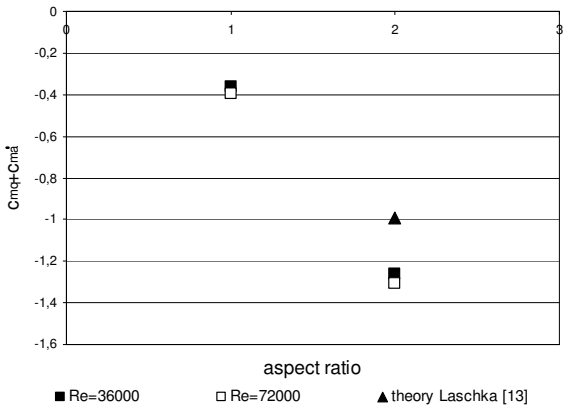

Fig. 23. Pitch moment damping, α_0=0, Re=36000 and 72000, k=0.25

6. CONCLUSION

A new test facility to investigate low Reynolds number unsteady aerodynamics, relevant for Micro Air Vehicles is presented. The test rig allows to determine dynamic distributions of aerodynamic coefficients. Furthermore a data evaluation method to determine dynamic derivatives has been verified.

The results of first measurements of static and dynamic aerodynamic forces and moments of four different MAV wings are presented. The effect of Reynolds number, aspect ratio and also flexibility of the wing is discussed.

It is found wings with small aspect ratio generate aerodynamic effects which need further investigations. These should focus on the influence of Reynolds number, wing planform and the reduced frequency k. Also aerodynamic flexible MAV wings should be investigated. Furthermore the unsteady aerodynamic coefficients for combined pitch and plunge motion should be examined in future experiments. For this kind of motion the presented data evaluation method has to be extended. The effect of sudden changes of the aerodynamic loads like in gusts can also be investigated using the presented test facility.

Since aerodynamic forces and moments of wings with small aspect ratio can not be assumed to be linear functions of model position and angular speed the linear approach of the existing data evaluation is probably not valid any more. Hence new non linear methods to determine dynamic derivatives should be established in the future.

In a next step also Particle Image Velocimetry measurements will be performed to investigate the flow field around different types of MAV wings to understand the structure of the unsteady wake of MAV wings with small aspect ratio as well as the behaviour of the wing tip vortices.

7. ACKNOWLEDGEMENT

The authors gratefully acknowledge funding by the project AUTOMAV of the German Aeronautics Research Programme during 2004-2006, and by DLR in 2007.

8. LITERATURE

[1] Shkarayev S, Null W, Wagner M, Development of Micro Air Vehicle Technology With In-Flight Adaptive-Wing Structure, NASA/CR-2004-213271, 2004.

[2] Lian Y, Shvy W, Haftka R: Shape optimization of a Membrane Wind for Micro Air Vehicle, AIAA Paper No. AIAA-2003-0106, Presented at the 41th AIAA Aerospace Sciences Meeting and Exhibit, Reno, NV, January, 2003.

[3] Grasmeyer JM, Kaennon MT: Development of the Black Widow micro air vehicle, AIAA Paper No. AIAA-2001-0127, Presented at the 39th AIAA Aerospace Sciences Meeting and Exhibit, Reno, NV, January, 2001.

[4] Ekaerinaris JA, Chandrasekhara MS, Platzer MF: Analysis of Low Reynolds Number Airfoil Flows, Journal of Aircraft Vol. 32, no 3, pp 625-630, 1995.

[5] Ramamurti R, Sandberg W: Simulation of the Dyanmics of Micro Air Vehicles, AIAA Paper No. AIAA-2000-0896, Presented at the 38th AIAA Aerospace Sciences Meeting and Exhibit, Reno, NV, January, 2000.

[6] Swanson T, Isaac KM: Low Re, High Wing Aerodynamics for Micro Air Vehicle Applications, AIAA paper 2008-421, 2008.

[7] Sunada S, Kawachi K, Matsumoto A: Unsteady forces and a two-dimensional Wing in Plunging and Pitching Motions, AIAA Journal 2001, vol. 39, no 7, pp. 1230-1239, 2001.

[8] Hübner AR: Numerical Research of Dynamic Derivatives of unsteady moved Aircraft, VKI LS 2008-2, Experimental Determination of dynamic stability parameters, 2008.

[9] Smith M: Analysis of wind tunnel oscillatory data of the X-31a aircraft. Technical Report NASA/CR-1999-028725, NASA, 1999.

[10] Loeser, Th: Experimental Research of Dynamic Derivatives of Unsteady Moved Aircraft, VKI LS 2008-2, Experimental Determination of dynamic stability parameters, 2008.

[11] Dornier GmbH. Oszillierende Derivativawaage für die 3m Unterschallwindkanäle der BRD, Forschungs-bericht 76/1 3B, 1976.

[12] Schlichting H, Truckenbrodt E: Aerodynamik des Flugzeuges Band 2, 3. Auflage, pp. 52-53, Springer Verlag, 2001.

[13] Laschka B: Zur Theorie der harmonisch schwingenden tragenden Fläche bei Unterschallströmung, Z.Flugwiss, 11, Heft 7, pp 265-292, 1963.